Biological Psychiatry: GOS

# Intrinsic Gene Expression Correlates of the Biophysically Modeled Diffusion Magnetic Resonance Imaging Signal

Ajay P. Singh, Michael Fromandi, Daniel Pimentel-Alarcón, Donna M. Werling, Audrey P. Gasch, and John-Paul J. Yu

**ABSTRACT**

Magnetic resonance imaging (MRI) is a powerful tool to identify the structural and functional correlates of neurological illness but provides limited insight into molecular neurobiology. Using rat genetic models of autism spectrum disorder, we show that image texture–processed neurite orientation dispersion and density imaging (NODDI) diffusion MRI possesses an intrinsic relationship with gene expression that corresponds to the biophysically modeled cellular compartments of the NODDI diffusion signal. Specifically, we demonstrate that neurite density index and orientation dispersion index signals are correlated with intracellular and extracellular gene expression, respectively. Moreover, we further demonstrate that these imaging signals correlate with genes specifically relevant to the etiopathogenesis of autism spectrum disorder. In sum, our data suggest fundamental relationships between gene expression and diffusion MRI, implicating the potential of diffusion MRI to probe causal neurobiological mechanisms in neuroimaging phenotypes in autism spectrum disorder.

https://doi.org/10.1016/j.bpsgos.2024.100430

A fundamental goal of neuroscience is to understand the structure and function of the brain and the neurobiological correlates that give rise to cognition and behavior. Magnetic resonance imaging (MRI) provides a powerful tool to study the living brain and to uncover the neural substrates of neurological, neurocognitive, and neuropsychiatric illness. However, modern neuroimaging techniques only indirectly measure underlying pathology by producing imaging phenotypes, which serve as nonspecific macroscale proxies for the molecular processes that drive pathological changes in the brain (1). Because brain architecture and activity are governed by transcriptomic measures (2–5), a fundamental understanding of the relationship between the MR signal and gene expression is critically needed to facilitate an in vivo understanding of the brain in health and disease.

To correlate measures of the MR signal with gene expression, a diffusion MRI (dMRI) method like neurite orientation dispersion and density imaging (NODDI) (6) serves as a natural departure point. Unlike conventional structural (T1, T2) or functional (blood oxygen level–dependent) neuroimaging techniques, NODDI is at once sensitive and directly related to underlying molecular and cellular phenomena (7–9) and possesses remarkable sensitivity to molecular neurobiology (7–11). With extensive evidence supporting the robust correlation between gene expression and brain cellular histology (12–14) and, similarly, between brain cellular histology and dMRI (11,15–19), we reasoned that dMRI measures would be correlated with and thus predictive of gene expression signatures and their underlying neurobiology (Figure 1A). Furthermore, because the NODDI signal itself is spatially defined (e.g., neurite density index [NDI], restricted diffusion, intracellular; orientation dispersion index [ODI], hindered diffusion, extracellular), putative correlations of the NODDI signal with gene expression would be expected to correspond with biological processes that are themselves spatially distinct.

Although techniques like NODDI are sensitive to neurobiology, they remain nonspecific. This nonspecificity arises partly from how quantitative MRI is processed. Typically, only a few MR measures (e.g., mean intensity, cortical thickness) are reported for a given contrast, and the limited number of MR measurements made restricts the generation of specific correlations between MRI measures, gene expression, and neuropathology. Previous work has sought to utilize multiple MR contrasts to expand the number of measurements available to correlate with genetic data (20,21). Here, we utilized image texture analysis (i.e., radiomics) instead, which, in the process of quantifying the spatial arrangement of intensities in an image, generates over 80 quantitative imaging measures from a single MR contrast (Figure 1B). The availability of this expanded set of parameters may allow us to more specifically identify MR signal–gene expression correlates.

To test this premise, we turned to a reduced system: the wild-type rat and *Nrxn1*$^{-/-}$, *Pten*$^{-/+}$, *Fmr1*$^{-/y}$ genetic rat models of autism spectrum disorder (ASD). We specifically





ISSN: 2667-1743

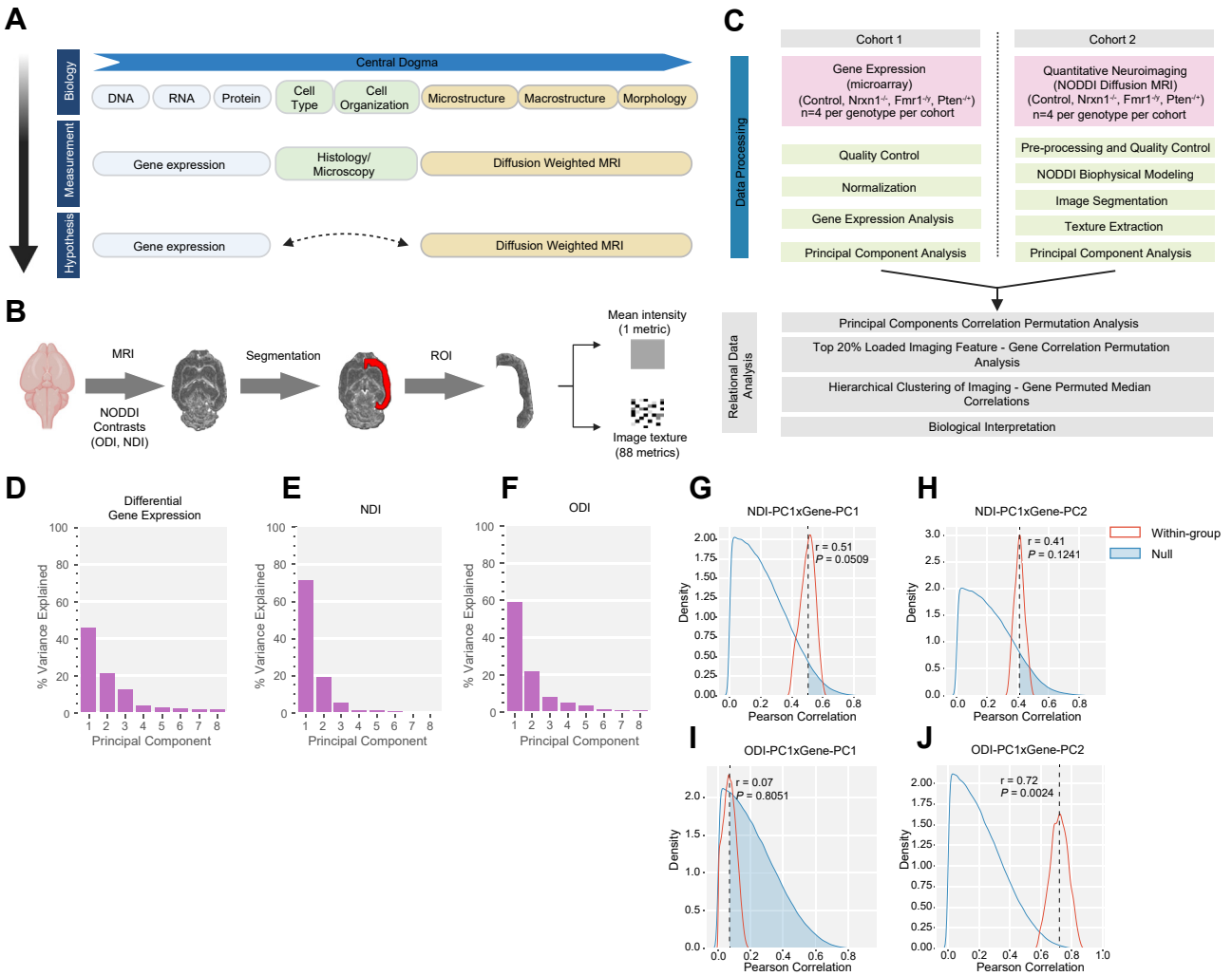


**Figure 1.** NDI and ODI signals are correlated with differential gene expression. **(A)** Theoretical framework depicting the canonical biological relationships between cellular histology and brain structure and the hypothesized relationship between quantitative diffusion MRI and gene expression. **(B)** Overview of different imaging analysis pipelines contrasting standard mean intensity ROI studies (top) to a texture-based approach (bottom) highlights the increased number of quantitative parameters that can be extracted per segmented ROI when utilizing a texture-based approach (1 vs. 88 per imaging contrast). **(C)** Data processing and analysis pipelines for determining the relationship between and biological interpretation of gene expression analysis and quantitative diffusion MRI. PC analysis of **(D)** differential gene expression, **(E)** NDI texture features, and **(F)** ODI texture features was performed, and the percentage (%) variance explained for all PCs was graphed. **(G–J)** For each permuted correlation between the imaging signal (NDI-PC1; ODI-PC1) and differential gene expression (gene-PC1; gene-PC2), the absolute value of that correlation was calculated. The distribution of these correlation values is presented as a kernel density plot for within-group (red) and null (blue) permutations. The dotted black line denotes the median correlation (*r*) for within-group permutations. The shaded blue area indicates the fraction of null values greater than *r* and is used to calculate a permutation-based *p* value. MRI, magnetic resonance imaging; NDI, neurite density index; NODDI, neurite orientation dispersion and density index; ODI, orientation dispersion index; PC, principal component; ROI, region of interest.

chose 3 genetically distinct ASD models as the basis for this study because of the presence of both neuronal (e.g., synaptic) (22–24) and extraneuronal (e.g., perineuronal net deposition) (25,26) processes in the pathophysiology of ASD. This provides an opportune test of the biological specificity of the NODDI biophysical model and its correlation with biological processes that are altered differently across genetic backgrounds (Figure 1C).

## METHODS AND MATERIALS

### Animals

All procedures were approved by the Institutional Animal Care and Use Committee at our institution. Male Sprague Dawley rats (300–325 g; Charles River) were pair housed in clear cages (lights on for 12 hours at 7 AM) with ad libitum access to food and water; experiments were performed between 10 AM and 3 PM.

*Fmr1*$^{-/y}$, *Nrxn1*$^{-/-}$, and *Pten*$^{-/+}$ genetic knockout rat models of ASD were commercially obtained (Horizon Discovery). All models were generated via zinc finger nuclease genome editing that yielded a hemizygous, homozygous, and heterozygous genotype on the outbred Sprague Dawley background, respectively.

## Microarray Gene Expression Analysis

Bulk RNA was collected from the left neocortex of *Fmr1*$^{-/y}$, *Nrxn1*$^{-/-}$, and *Pten*$^{-/+}$ rats and wild-type controls ($n$ = 4 per group, Sprague Dawley background males, aged to postnatal day 45) using Qiagen RNEasy Midi Kit (75144; Qiagen) and analyzed using the Rat Gene 2.0 ST Affymetrix microarray (902124; Thermo Fisher Scientific) to collect exome-wide gene expression data for all samples. The microarray data was analyzed using R version 4.2.2 using the libraries *pd.rgene.2.0.st* (version 3.14.1) (27), *oligo* (version 1.62.0) (28), *arrayQualityMetrics* (version 3.54.0) (29), and *limma* (version 3.54.0) (30). Preprocessing was performed using robust multichip average preprocessing included in the *oligo* package, which performs background subtraction and quantile normalization across all samples. *arrayQualityMetrics* was then run on the normalized data to identify possible outlier samples. The *Nrxn1*$^{-/-}$ sample N_g_1 was an outlier due to differences in its overall average gene expression identified visually through principal component (PC) analysis and inspection of boxplot distributions and statistically using the Kolmogorov-Smirnov test. After removing that sample, genes were filtered using a median intensity threshold of 4 to remove lowly expressed genes. Remaining genes were regressed on the 4 genotypes using the *limma lm* function. No additional covariates were considered because all samples were taken at the same age, had the same sex, and were run on the same microarray experiment. Empirical Bayes was used to calculate the moderated $F$ statistics of differential expression from the linear model (31). The *Limma toptable* function was used to generate a list of differentially expressed genes. Genes were considered significant if the false discovery rate–corrected $p$ value for the linear model of that gene was $<.05$. In total, 4399 annotated genes were identified as statistically significant (Figure S1).

## MRI Acquisition and Image Processing

A cohort of animals, separate from those used for microarray analysis (*Nrxn1*$^{-/-}$, *Pten*$^{-/+}$, *Fmr1*$^{-/y}$ [$n$ = 4 each], and their controls [$n$ = 4]) at postnatal day 45 were transcardially perfused with ice-cold phosphate-buffered saline followed by 4% paraformaldehyde (32). Following dissection from the cranial vault, fixed brains were then stored in 4% paraformaldehyde for 24 hours, whereupon they were serially rinsed in 1× phosphate-buffered saline for 48 hours prior to imaging. The brains were placed in a custom-built holder and immersed in Fluorinert for imaging (FC-3283; 3M). Brains were imaged with a 4.7T Agilent MRI system with a 3.5 cm diameter quadrature volume radiofrequency coil. Multislice, diffusion-weighted, spin echo images were used to acquire 10 non–diffusion-weighted interleaved images ($b$ = 0 s/mm$^2$) and 75 diffusion-weighted images (25: $b$ = 800 s/mm$^2$, 50: $b$ = 2000 s/mm$^2$) using noncollinear diffusion-weighting directions. Other imaging parameters were as follows: echo time/repetition time = 24.17/2000 ms, field of view = 30 × 30 mm$^2$, matrix = 192 × 192 reconstructed to 256 × 256 for an isotropic voxel size of 0.25 mm over 2 signal averages; d = 6 ms; D = 12.20 ms; temperature = 20−21 °C; total acquisition time 21 hours, 30 minutes. Raw data files were converted to NIfTI format, and FSL was used to correct for eddy current artifacts. FSL output volumes were converted to NIfTI tensor format for use. Tensors were reconstructed with the DTI-TK software package (33). Each imaged brain underwent spatial normalization to a diffusion tensor imaging–based rat brain atlas (34). Diffusion data were then fitted to the NODDI model using the Microstructure Diffusion Toolbox (Figure S2) (35). Regions of interest (ROIs) were then masked and segmented using the atlas coordinates. The neocortex ROI was processed using the *pyradiomics* (version 3.1.0) package (36) to extract image texture features with a fixed bin width of 0.1 (37,38) and feature extraction was performed for 18 first-order statistics, 24 gray-level cooccurrence matrix, 14 gray-level dependence matrix, 16 gray-level run length matrix, and 16 gray-level size zone matrix radiomic features. Analytical pipelines were specifically designed for imaging data collected from fixed samples (e.g., using recommended diffusivity assumptions $d_{\parallel} = 0.6 \times 10^{-3}$ mm$^2$/s and the $d_{iso} = 2 \times 10^{-3}$ mm$^2$/s) and using the WatsonSHStickTortIsoVIsoDot_B0 fitting model as recommended.

## Permutation PC Correlation Analysis Between Imaging and Gene Expression Datasets

Values for each of the 4399 differentially expressed genes and the 84 nonzero NDI and 86 nonzero ODI imaging features were first $\log_2$ transformed and then centered to the mean value across all samples. PC analysis was performed on each dataset across all 4 genotypes. To test whether the imaging datasets and gene expression dataset explain the variance between the animal models in a related manner, the first 2 PCs of the gene expression data were correlated with the first PC of the NDI and ODI imaging feature datasets using Pearson's correlations. These PCs were chosen because they described the most variance in the data. Correlation of imaging PCs with those gene PCs would suggest that the imaging PCs can explain at least part of the relationship captured by the gene expression data. Specifically, the PC vector coefficients in the datasets were correlated ($n$ = 15 for gene expression; $n$ = 16 for imaging). Because the 2 datasets were generated from different cohorts of animals with the same genotypes, we performed a permutation test to calculate the distribution of Pearson's correlations in the imaging and gene expression PCs. Samples were permuted within each genotype (within-group distribution; $k = [4p4]^3 \times [4p3] = 331{,}776$) and compared with the distribution of random permutations in which genotype groups were not maintained across the imaging and gene expression datasets. Due to computational constraints, 1 million permutations were randomly sampled without replacement to estimate the null distribution (k = 1,000,000). Because the sign on PC vectors is uninformative, we took the absolute value of each calculated correlation. To assess the strength of the correlations between the imaging and gene expression datasets, we calculated the probability of null permutations with a correlation greater than or equal to the median of the observed within-group distribution and reported

this as $p$. Smaller $p$ values indicated that the correlation between the PCs tested was less likely to have occurred by chance and is demonstrative of a strong, genotype-driven correlation between the signals. All PC calculation and correlation permutations were performed using *sklearn* (version 1.1.1) (39), *NumPy* (version 1.23.0) (40), and *pandas* (version 1.1.4) (41) in python version 3.10.5.

### Hierarchical Clustering of Correlated Genes and Features and Metascape Gene Ontology Analysis

To identify which imaging features and genes underlie the correlation between PCs, the top 20% of loaded genes and features were chosen based on selecting the genes and features with the highest absolute value of the PC loadings in the tested PCs. Choosing the top 20% of the loaded genes in each PC enabled interpretation of the biology captured in each PC beyond genotype differences. Similarly, the top 20% of imaging features in our imaging dataset were likely the most informative about the underlying biological signal. This identified 880 genes for the first and second PC and 17 and 18 imaging features from the first NDI and ODI PCs, respectively. Again, due to the lack of intrinsic pairing between the datasets for each animal, a permutation analysis was performed, as described above. Due to computational constraints, 13,000 of the 331,776 possible permutations were randomly sampled without replacement to estimate the distribution of correlations between a feature and a gene. The median correlation for each gene-imaging feature was compiled and organized by hierarchical clustering using the uncentered correlation distance metric and centroid linkage algorithm from the Gene Cluster 3.0 software (42). Dendrograms and heatmaps of the median correlation of gene-imaging feature data were drawn using Java TreeView 1.2 (43).

Clusters were manually selected based on the hierarchical clustering to identify the set of genes that most highly correlated with the imaging features. Genes in these clusters were then analyzed using gene ontology (GO) enrichment with the cellular component ontology terms. Enrichment for cellular component ontology was specifically chosen to identify which biophysical elements of the cellular environment most specifically influence each imaging signal. Metascape (44) was used to perform GO enrichment against the background of all genes effectively measured by the microarray experiment. GO term enrichment was defined as having a cumulative hypergeometric distribution $p$ value $< 10^{-6}$. GO terms that did not have a fold enrichment of at least 1.5 or a minimum of 3 genes represented within the term were not considered for enrichment. Heatmaps of enriched GO terms were generated using kappa scores defined from the overlap of genes between GO term gene sets used as the similarity metric for performing hierarchical clustering on the enriched terms. Subtrees with a similarity $>0.3$ were considered a cluster. The most statistically significant term within a cluster was chosen to represent the cluster. GO enrichment heatmaps were created using Metascape.

### Autism Association Score

Using the genome-wide prediction for ASD risk scores generated by Krishnan *et al.* (45), we ranked each gene with its relative ASD risk score. Then, we compared the mean relative ASD risk of the GO term–enriched NODDI-associated differentially expressed genes to the mean relative ASD risk across the genome and all autism-associated genes identified by the Simons Foundation Autism Research Initiative. More positive relative ASD risk scores indicated a higher association with ASD pathogenesis.

## RESULTS

### NODDI Diffusion Signal Is Correlated to Gene Expression in the Brain

In the gene expression dataset, PCs 1 and 2 described the majority of the variance and clearly segregated the 4 genotypes into distinct, genotype-specific clusters, highlighting that genotype differences drove the variance in the gene expression dataset (Figure 1D and Figure S3A). In the NDI and ODI texture datasets, PC1 in each dataset described the majority of their respective variances (Figure 1E, F and Figure S3B, C). The correlations of the PCs between imaging and gene expression datasets were calculated. PC1 of NDI was highly predictive of PC1 of gene expression (Figure 1G) (NDI-PC1 $\times$ gene-PC1, median $r = 0.506$, permutation test $p = .0508$). Conversely, PC1 of NDI was only moderately predictive of PC2 of gene expression (Figure 1H) (NDI-PC1 $\times$ gene-PC2; median $r = 0.4108$, permutation test $p = .1241$). We also found that PC1 of ODI demonstrated a very weak correlation with PC1 of gene expression (Figure 1I) (ODI-PC1 $\times$ gene-PC1; median $r = 0.0694$, permutation test $p$ value = .8051) and a very strong correlation to PC2 of gene expression (Figure 1J) (ODI-PC1 $\times$ gene-PC2; median $r = 0.7206$, permutation test $p$ value = .0024). Texture features enabled improved specificity when compared with correlating gene PCs with mean intensity alone (Figure S4). All within-group permutations had nonrandom distributions, and their median $r$ values demonstrated the similarity of information captured between imaging and gene expression signals from each PC.

### NDI and ODI Are Associated With Specific Gene Expression Sets Relevant to ASD Pathophysiology

To biologically contextualize the imaging and gene expression PCs that were most strongly predictive of each other (NDI-PC1:gene-PC1; ODI-PC1:gene-PC2), we extracted the top 20% of genes and image texture features loaded in each PC (880 genes per gene-PC; 17 NDI and 18 ODI texture features) and performed unsupervised hierarchical clustering of the median correlations for each feature pair, creating gene clusters defined by their correlations with the imaging features (Figure 2A, B). Of the 4 major gene clusters identified, 3 were statistically enriched for GO cellular components (46) ($p < 10^{-6}$, hypergeometric test) (Figure 2C). The NDI GO terms clustered separately from the ODI GO terms, highlighting the biological specificity of the cellular components associated with each imaging signal. The largest cluster identified (ODI-PC1 $\times$ gene-PC2, cluster 1) was enriched for extracellular matrix and collagen trimers, consistent with the extracellular-derived ODI signal and biologically consistent with the role of the extracellular matrix and perineuronal nets in the neuropathogenesis of ASD (25,26). In contrast, NDI-PC1 $\times$ gene-PC1 cluster 2 was significantly enriched for synaptic

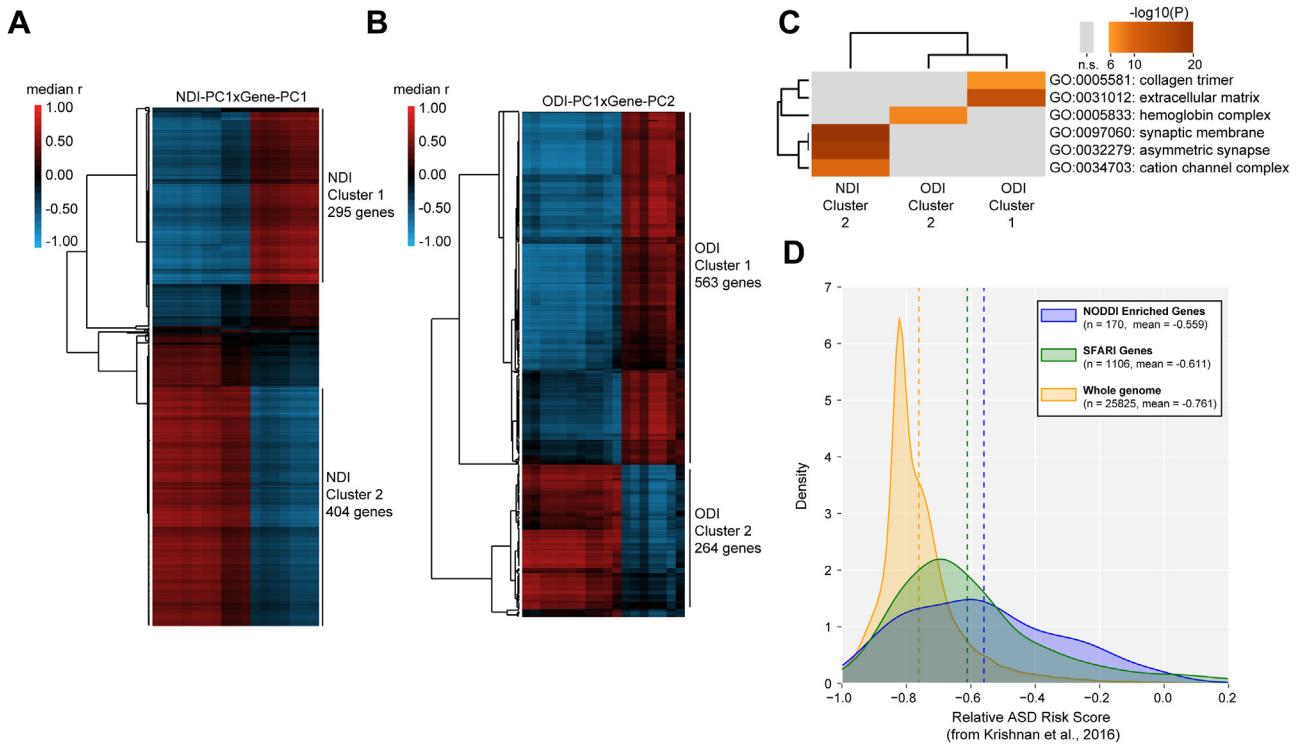


**Figure 2.** Clustering gene-feature correlations highlights specificity of NDI and ODI signals to underlying cellular components and risk for ASD. Hierarchical clustering and heatmaps of median *r* correlation values between **(A)** the top 20% of loaded NDI-PC1 features (columns) and the top 20% of loaded gene-PC1 genes (rows) and **(B)** the top 20% of loaded ODI-PC1 features (columns) and the top 20% of loaded PC2 genes (rows). Clusters were selected following the dendrogram for downstream GO analysis. **(C)** Heatmap of significantly enriched cellular component GO terms (hypergeometric $p < 10^{-6}$). Three of the 4 clusters enrich for cellular component GO terms; NDI cluster 1 did not significantly enrich and thus is not visualized. NDI and ODI clusters were associated with cellular component GO terms that were consistent with their biophysically modeled compartment (e.g., neuronal [NDI]; extraneuronal [ODI]). Displayed values are $-\log_{10}$ of the enrichment *p* value. **(D)** Distributions of individual gene risk scores for ASD across 3 different gene sets: whole genome (orange), SFARI Human Gene Module (green), and the GO term–associated NODDI enriched genes (blue). Vertical dotted lines indicate the respective relative mean risk scores for the genes in each distribution. More positive scores indicate a greater association of genetic risk with ASD. ASD risk scores for each gene are calculated from Krishnan *et al.*'s genome-wide prediction for ASD risk (45). ASD, autism spectrum disorder; GO, gene ontology; NDI, neurite density index; NODDI, neurite orientation dispersion and density index; n.s., not significant; ODI, orientation dispersion index; PC, principal component; SFARI, Simons Foundation Autism Research Initiative.

membrane, asymmetrical synapses, and cation channel complex, consistent with the intraneuronal/intracellularly derived NDI signal (see Supplemental Data for gene lists).

The genes from NDI cluster 2 and ODI clusters 1 and 2 that significantly associated with GO terms represent the most biologically interpretable genes that correlated with our NODDI signals. Next, we calculated the relative ASD risk score for each gene in these clusters using a genome-wide prediction tool for ASD risk devised by Krishnan *et al.* (45). Compared to the genome-wide average and autism-associated genes identified by the Simons Foundation Autism Research Initiative, our extracted gene set demonstrated a higher average ASD risk score, underscoring the biological relevance that our selected genes have to autism pathogenesis (Figure 2D and Figure S5).

## DISCUSSION

A more precise relationship between the MR signal and gene expression has been sought for a long time. Here, we uncover and describe a previously undetected intrinsic relationship between the biophysically modeled diffusion signal and gene expression in the brain. Unlike commonly reported neuroimaging transcriptomics studies (47–49), we opted instead to test our novel approach in a rodent model rather than using human data. By testing imaging-transcriptomic correlations in a model system, more direct associations of the imaging signal with molecular biology can be made, and specific molecular mechanisms can be explored that are otherwise too difficult to test in human datasets or through atlas-based approaches (50,51). Our findings reveal that the spatially defined NODDI signal is strongly correlated with gene expression of cellular components that correspond to their respective NODDI-defined biophysical compartment (NDI with gene-PC1 [intracellular]; ODI with gene-PC2 [extracellular]). These findings underscore the biologically derived relationship between imaging and gene expression, demonstrating how the NDI and ODI diffusion signals specifically correlate with different gene expression patterns. Lastly, our results suggest more specificity in the ODI signal, which is consistent with previous work that demonstrated the sensitivity and specificity of the ODI signal (52).

Potential limitations of our study include the use of ex vivo imaging. Although ex vivo studies do not directly recapitulate in vivo imaging (53,54), ex vivo approaches, after accounting for tissue fixation when fitting our NODDI modeling parameters, provide higher signal-to-noise ratios and greater spatial resolution due to the capacity for longer scanning times. While most genetic autism rodent model studies have used mice, we chose to study genetic rat models because there has been a push in neurobiology studies to focus on rats, especially for complex communication disorders such as ASD (55–57). Additionally, to our knowledge, our study is the first cross-model transcriptomic analysis of monogenetic rat models of autism. It is also the first cortical gene expression study from the *Nrxn1* and *Pten* rat models.

As we continue to refine our understanding of the MR signal and gene expression relationship, future applications would see MRI being used to directly probe changes in gene expression, thereby allowing us to noninvasively identify potential alterations in the molecular neurobiology of patients. Defining patients with neurological illness based on molecular phenotypes rather than on clinical symptoms would provide needed biological specificity to the clinical neurosciences and, importantly, would support continued efforts toward precision treatment based on underlying biological mechanisms.

## ACKNOWLEDGMENTS AND DISCLOSURES

This work was supported by the University of Wisconsin-Madison School of Medicine and Public Health and Department of Radiology start-up funds and by the Brain Foundation and the O'Sullivan Foundation (to J-PJY).

We thank B. Rauch, M.S., for outstanding small animal imaging support through the Small Animal Imaging at the University of Wisconsin Carbone Cancer Center.

The authors report no biomedical financial interests or potential conflicts of interests.

## ARTICLE INFORMATION

From the Graduate Program in Cellular and Molecular Biology, University of Wisconsin-Madison, Madison, Wisconsin (APS); Department of Radiology, University of Wisconsin School of Medicine and Public Health, Madison, Wisconsin (MF, J-PJY); Department of Biostatistics, University of Wisconsin-Madison, Madison, Wisconsin (DP-A); Waisman Center, University of Wisconsin-Madison, Madison, Wisconsin (DMW); Laboratory of Genetics, University of Wisconsin-Madison, Madison, Wisconsin (DMW, APG); Center for Genomic Science Innovation, University of Wisconsin-Madison, Madison, Wisconsin (APG); Department of Biomedical Engineering, University of Wisconsin-Madison, Madison, Wisconsin (J-PJY); and Department of Psychiatry, University of Wisconsin School of Medicine and Public Health, Madison, Wisconsin (J-PJY).

Address correspondence to John-Paul J. Yu, M.D., Ph.D., at jp.yu@wisc.edu.

Received Jul 29, 2024; revised Oct 18, 2024; accepted Dec 1, 2024.

Supplementary material cited in this article is available online at https://doi.org/10.1016/j.bpsgos.2024.100430.

## REFERENCES

1. Arnatkeviciute A, Fulcher BD, Bellgrove MA, Fornito A (2022): Imaging transcriptomics of brain disorders. Biol Psychiatry Glob Open Sci 2:319–331.
2. Hawrylycz M, Miller JA, Menon V, Feng D, Dolbeare T, Guillozet-Bongaarts AL, *et al.* (2015): Canonical genetic signatures of the adult human brain. Nat Neurosci 18:1832–1844.
3. Hawrylycz MJ, Lein ES, Guillozet-Bongaarts AL, Shen EH, Ng L, Miller JA, *et al.* (2012): An anatomically comprehensive atlas of the adult human brain transcriptome. Nature 489:391–399.
4. Berto S, Treacher AH, Caglayan E, Luo D, Haney JR, Gandal MJ, *et al.* (2022): Association between resting-state functional brain connectivity and gene expression is altered in autism spectrum disorder. Nat Commun 13:3328.
5. Wen J, Goyal MS, Astafiev SV, Raichle ME, Yablonskiy DA (2018): Genetically defined cellular correlates of the baseline brain MRI signal. Proc Natl Acad Sci U S A 115:E9727–E9736.
6. Zhang H, Schneider T, Wheeler-Kingshott CA, Alexander DC (2012): NODDI: Practical in vivo neurite orientation dispersion and density imaging of the human brain. Neuroimage 61:1000–1016.
7. Martinez-Heras E, Grussu F, Prados F, Solana E, Llufriu S (2021): Diffusion-weighted imaging: Recent advances and applications. Semin Ultrasound CT MR 42:490–506.
8. Alexander DC, Dyrby TB, Nilsson M, Zhang H (2019): Imaging brain microstructure with diffusion MRI: Practicality and applications. NMR Biomed 32:e3841.
9. Afzali M, Pieciak T, Newman S, Garyfallidis E, Özarslan E, Cheng H, Jones DK (2021): The sensitivity of diffusion MRI to microstructural properties and experimental factors. J Neurosci Methods 347:108951.
10. Yi SY, Stowe NA, Barnett BR, Dodd K, Yu JJ (2020): Microglial density alters measures of axonal integrity and structural connectivity. Biol Psychiatry Cogn Neurosci Neuroimaging 5:1061–1068.
11. Yi SY, Barnett BR, Torres-Velázquez M, Zhang Y, Hurley SA, Rowley PA, *et al.* (2019): Detecting microglial density with quantitative multi-compartment diffusion MRI. Front Neurosci 13:81.
12. Pecheva D, Lee A, Poh JS, Chong YS, Shek LP, Gluckman PD, *et al.* (2020): Neural transcription correlates of multimodal cortical phenotypes during development. Cereb Cortex 30:2740–2754.
13. Darmanis S, Sloan SA, Zhang Y, Enge M, Caneda C, Shuer LM, *et al.* (2015): A survey of human brain transcriptome diversity at the single cell level. Proc Natl Acad Sci U S A 112:7285–7290.
14. French L, Pavlidis P (2011): Relationships between gene expression and brain wiring in the adult rodent brain. PLoS Comput Biol 7: e1001049.
15. Garcia-Hernandez R, Cerdán Cerdá A, Trouve Carpena A, Drakesmith M, Koller K, Jones DK, *et al.* (2022): Mapping microglia and astrocyte activation in vivo using diffusion MRI. Sci Adv 8:eabq2923.
16. Benjamini D, Priemer DS, Perl DP, Brody DL, Basser PJ (2023): Mapping astrogliosis in the individual human brain using multidimensional MRI. Brain 146:1212–1226.
17. Sepehrband F, Clark KA, Ullmann JFP, Kurniawan ND, Leanage G, Reutens DC, Yang Z (2015): Brain tissue compartment density estimated using diffusion-weighted MRI yields tissue parameters consistent with histology. Hum Brain Mapp 36:3687–3702.
18. Schilling KG, Janve V, Gao Y, Stepniewska I, Landman BA, Anderson AW (2018): Histological validation of diffusion MRI fiber orientation distributions and dispersion. Neuroimage 165:200–221.
19. Taquet M, Jankovski A, Rensonnet G, Jacobs D, des Rieux A, Macq B, *et al.* (2019): Extra-axonal restricted diffusion as an in-vivo marker of reactive microglia. Sci Rep 9:13874.
20. Hu LS, D'Angelo F, Weiskittel TM, Caruso FP, Fortin Ensign SP, Blomquist MR, *et al.* (2023): Integrated molecular and multiparametric MRI mapping of high-grade glioma identifies regional biologic signatures. Nat Commun 14:6066.
21. Stoyanova R, Pollack A, Takhar M, Lynne C, Parra N, Lam LLC, *et al.* (2016): Association of multiparametric MRI quantitative imaging features with prostate cancer gene expression in MRI-targeted prostate biopsies. Oncotarget 7:53362–53376.
22. Baudouin SJ, Gaudias J, Gerharz S, Hatstatt L, Zhou K, Punnakkal P, *et al.* (2012): Shared synaptic pathophysiology in syndromic and nonsyndromic rodent models of autism. Science 338:128–132.
23. Greenblatt EJ, Spradling AC (2018): Fragile X mental retardation 1 gene enhances the translation of large autism-related proteins. Science 361:709–712.
24. Yi F, Danko T, Botelho SC, Patzke C, Pak C, Wernig M, Südhof TC (2016): Autism-associated SHANK3 haploinsufficiency causes Ih channelopathy in human neurons. Science 352:aaf2669.

25. Cope EC, Zych AD, Katchur NJ, Waters RC, Laham BJ, Diethorn EJ, *et al.* (2022): Atypical perineuronal nets in the CA2 region interfere with social memory in a mouse model of social dysfunction. Mol Psychiatry 27:3520–3531.
26. Murthy S, Kane GA, Katchur NJ, Lara Mejia PS, Obiofuma G, Buschman TJ, *et al.* (2019): Perineuronal nets, inhibitory interneurons, and anxiety-related ventral hippocampal neuronal oscillations are altered by early life adversity. Biol Psychiatry 85:1011–1020.
27. Carvalho B (2015): Platform Design Info for Affymetrix RaGene-2_0-st. Available at: https://bioconductor.org/packages/release/data/annotation/html/pd.ragene.2.0.st.html. Accessed May 1, 2023.
28. Carvalho BS, Irizarry RA (2010): A framework for oligonucleotide microarray preprocessing. Bioinformatics 26:2363–2367.
29. Kauffmann A, Gentleman R, Huber W (2009): arrayQualityMetrics–A bioconductor package for quality assessment of microarray data. Bioinformatics 25:415–416.
30. Ritchie ME, Phipson B, Wu D, Hu Y, Law CW, Shi W, Smyth GK (2015): limma powers differential expression analyses for RNA-sequencing and microarray studies. Nucleic Acids Res 43:e47.
31. Smyth GK (2004): Linear models and empirical bayes methods for assessing differential expression in microarray experiments. Stat Appl Genet Mol Biol 3:Article3.
32. Gage GJ, Kipke DR, Shain W (2012): Whole animal perfusion fixation for rodents. J Vis Exp 65:e3564.
33. Keihaninejad S, Zhang H, Ryan NS, Malone IB, Modat M, Cardoso MJ, *et al.* (2013): An unbiased longitudinal analysis framework for tracking white matter changes using diffusion tensor imaging with application to Alzheimer's disease. Neuroimage 72:153–163.
34. Jiang Y, Johnson GA (2011): Microscopic diffusion tensor atlas of the mouse brain. Neuroimage 56:1235–1243.
35. Harms RL, Fritz FJ, Tobisch A, Goebel R, Roebroeck A (2017): Robust and fast nonlinear optimization of diffusion MRI microstructure models. Neuroimage 155:82–96.
36. Van Griethuysen JJM, Fedorov A, Parmar C, Hosny A, Aucoin N, Narayan V, *et al.* (2017): Computational radiomics system to decode the radiographic phenotype. Cancer Res 77:e104–e107.
37. Zwanenburg A, Vallières M, Abdalah MA, Aerts HJWL, Andrearczyk V, Apte A, *et al.* (2020): The image biomarker standardization initiative: Standardized quantitative radiomics for high-throughput image-based phenotyping. Radiology 295:328–338.
38. Duron L, Balvay D, vande Perre S, Bouchouicha A, Savatovsky J, Sadik JC, *et al.* (2019): Gray-level discretization impacts reproducible MRI radiomics texture features. PLoS One 14:e0213459.
39. Pedregosa F, Varoquaux G, Gramfort A, Michel V, Thirion B, Grisel O, *et al.* (2011): Scikit-learn: Machine Learning in Python. J Mach Learn Res 12:2825–2830.
40. Harris CR, Millman KJ, van der Walt SJ, Gommers R, Virtanen P, Cournapeau D, *et al.* (2020): Array programming with NumPy. Nature 585:357–362.
41. Mckinney W (2010): Data structures for statistical computing in python. Proceedings of the Python in Science Conference 56–61.
42. de Hoon MJL, Imoto S, Nolan J, Miyano S (2004): Open source clustering software. Bioinformatics 20:1453–1454.
43. Saldanha AJ (2004): Java TreeView–Extensible visualization of microarray data. Bioinformatics 20:3246–3248.
44. Zhou Y, Zhou B, Pache L, Chang M, Khodabakhshi AH, Tanaseichuk O, *et al.* (2019): Metascape provides a biologist-oriented resource for the analysis of systems-level datasets. Nat Commun 10:1523.
45. Krishnan A, Zhang R, Yao V, Theesfeld CL, Wong AK, Tadych A, *et al.* (2016): Genome-wide prediction and functional characterization of the genetic basis of autism spectrum disorder. Nat Neurosci 19:1454–1462.
46. Cohen J (1960): A coefficient of agreement for nominal scales. Educ Psychol Meas 20:37–46.
47. Arnatkeviciute A, Markello RD, Fulcher BD, Misic B, Fornito A (2023): Toward best practices for imaging transcriptomics of the human brain. Biol Psychiatry 93:391–404.
48. Vértes PE, Rittman T, Whitaker KJ, Romero-Garcia R, Váša F, Kitzbichler MG, *et al.* (2016): Gene transcription profiles associated with inter-modular hubs and connection distance in human functional magnetic resonance imaging networks. Philos Trans R Soc Lond B Biol Sci 371:20150362.
49. Arnatkevičiūtė A, Fulcher BD, Fornito A (2019): A practical guide to linking brain-wide gene expression and neuroimaging data. Neuroimage 189:353–367.
50. Han X, Maharjan S, Chen J, Zhao Y, Qi Y, White LE, *et al.* (2024): High-resolution diffusion magnetic resonance imaging and spatial-transcriptomic in developing mouse brain. Neuroimage 297:120734.
51. Bledsoe X, Gamazon ER (2024): A transcriptomic atlas of the human brain reveals genetically determined aspects of neuropsychiatric health. Am J Hum Genet 111:1559–1572.
52. Timmers I, Roebroeck A, Bastiani M, Jansma B, Rubio-Gozalbo E, Zhang H (2016): Assessing microstructural substrates of white matter abnormalities: A comparative study using DTI and NODDI. PLoS One 11:e0167884.
53. Zhang J, Jones MV, McMahon MT, Mori S, Calabresi PA (2012): In vivo and ex vivo diffusion tensor imaging of cuprizone-induced demyelination in the Mouse corpus callosum. Magn Reson Med 67:750–759.
54. Vinh To X, Kurniawan ND, Cumming P, Nasrallah FA (2023): A cross-comparative analysis of in vivo versus ex vivo MRI indices in a mouse model of concussion. Brain Res 1820:148562.
55. Callaway E (2011): Rat models on the rise in autism research. Available at: https://www.nature.com/articles/nature.2011.9415. Accessed April 12, 2024.
56. Hrabovska SV, Salyha YT (2016): Animal models of autism spectrum disorders and behavioral techniques of their examination. Neurophysiology 48:380–388.
57. Clayton AL, Solis M (2021): SFARI workshop explores the use of rat models in autism research. Available at: https://www.sfari.org/2021/06/28/sfari-workshop-explores-the-use-of-rat-models-in-autism-research/. Accessed October 7, 2024.